

## Research Article

# Preparation of Improved p-n Junction NiO/TiO<sub>2</sub> Nanotubes for Solar-Energy-Driven Light Photocatalysis

Lan Ching Sim,<sup>1</sup> Kai Wern Ng,<sup>1</sup> Shaliza Ibrahim,<sup>1</sup> and Pichiah Saravanan<sup>1,2</sup>

<sup>1</sup> Environmental Engineering Laboratory, Department of Civil Engineering, Faculty of Engineering, University of Malaya, 50603 Kuala Lumpur, Malaysia

<sup>2</sup> Nanotechnology and Catalysis Research Centre (NANOCEN), University of Malaya, 50603 Kuala Lumpur, Malaysia

Correspondence should be addressed to Pichiah Saravanan; pichiahsaravanan@gmail.com

Received 28 November 2012; Revised 4 January 2013; Accepted 5 January 2013

Academic Editor: Xie Quan

Copyright © 2013 Lan Ching Sim et al. This is an open access article distributed under the Creative Commons Attribution License, which permits unrestricted use, distribution, and reproduction in any medium, provided the original work is properly cited.

Self-organized TiO<sub>2</sub> nanotubes (TNTs) with average inner diameter of 109 nm, wall thickness of 15 nm, and tube length of 7–10 μm were loaded with nickel oxide (NiO) nanoparticles via incipient wet impregnation method. The molar concentration of Ni(NO<sub>3</sub>)<sub>2</sub>·6H<sub>2</sub>O aqueous solution varied in a range of 0.5 M–2.5 M. The samples were characterized for crystalline phase, morphology, topography, chemical composition, Raman shift, and UV-Vis diffusion reflection properties. The finding shows that the loading of NiO did not influence the morphology, structure, and crystalline phase of TNTs but it exhibited significant effect on crystallite size and optical absorption properties. Further, the solar-energy-driven photocatalytic activity of NiO/TNTs and pure TNTs was evaluated by degrading methylene blue (MB). The results confirm that photocatalytic efficiency of NiO/TNTs is higher than that of TNTs.

## 1. Introduction

Self-organized and vertically oriented TiO<sub>2</sub> nanotubes (TNTs) are of great interest in photocatalytic applications due to their high surface-to-volume ratios, high surface area, good charge transport properties, and chemical stability [1]. Few studies have demonstrated TNTs with improved properties compared to other forms of TiO<sub>2</sub> for various applications including photocatalytic degradation of dyes and organic compounds, treatment of gaseous pollutants, water splitting, carbon dioxide (CO<sub>2</sub>) conversion to methane, and dye-sensitized solar cells [2–7]. However, the photocatalytic efficiency of TNTs is limited by fast recombination of photogenerated electron and hole pairs and its low visible light utilization. The wide bandgap energy of TiO<sub>2</sub> (3.2 eV for anatase and 3.0 eV for rutile) limits its excitation within the UV range of spectrum. The availability of such spectrum is marginal, that is, ≤5% of the whole solar spectrum in comparison to the visible light spectrum [8].

Many studies have been devoted to the improvement of TiO<sub>2</sub> photocatalytic activity towards solar light absorption.

The researchers have doped TiO<sub>2</sub> with metals such as Pt, Fe, Pd, Ag, and Ru [5, 9–12] and non-metals such as nitrogen (N) [9, 13], boron (B) [14], sulphur (S) [15], and carbon (C) [16] for higher photocatalytic activity in visible light region. Besides, TiO<sub>2</sub> can be coupled with semiconductors such as NiO [17], ZnO [18], CdS [19], PbS [20], SrTiO<sub>3</sub> [21], Fe<sub>2</sub>O<sub>3</sub> [10], and SnO<sub>2</sub> [22] to facilitate charge separation and extend the photoresponding range. In recent years, p-n junction photocatalysts such as NiO/TiO<sub>2</sub>, NiO/InVO<sub>4</sub>, NiO/ZnO, and V/TiO<sub>2</sub> have had more focus due to their improved charge separations [23–27]. NiO is a p-type semiconductor [28, 29] frequently used as a cocatalyst loaded with various n-type semiconductors because of its high p-type concentration, higher hole mobility, and cost effectiveness [30]. In addition, the presence of NiO promotes the separation of electron and hole pairs through the electric junction field and favours the interfacial charge transfer [31–33].

Quite a few research groups have investigated the utilization of NiO-doped TiO<sub>2</sub> as hydrogen evolution sites from photocatalytic water splitting [23, 34]. However, the studies on the solar-energy-driven photocatalytic activity

TABLE 1: Experimental conditions and elemental composition of the prepared composite samples.

| Sample           | Ni(NO <sub>3</sub> ) <sub>2</sub> ·6H <sub>2</sub> O (M) | EDS                         |      |     |
|------------------|--|-----------------------------|------|-----|
|                  |  | Elemental composition (wt%) |      |     |
|                  |  | Ti                          | O    | Ni  |
| TNTs             | 0  | 58.6                        | 41.4 | 0   |
| NiO/TNTs (0.5 M) | 0.5  | 59.3                        | 39.9 | 0.8 |
| NiO/TNTs (1.5 M) | 1.5  | 58.9                        | 40.1 | 1   |
| NiO/TNTs (2.5 M) | 2.5  | 59.1                        | 37.5 | 3.4 |

are still limited. In our present work, enhanced solar-light-induced photocatalytic active p-n junction of NiO/TNTs photocatalysts was prepared via simple incipient wet impregnation method, and its materials chemistry was investigated. Methylene blue (MB) dye was chosen as the model pollutant to evaluate the photocatalytic activity of the pure and NiO-loaded TNTs. Direct solar light was employed to illustrate the possibility of solar light utilization.

## 2. Experimental

**2.1. Preparation of TNTs.** All the chemical reagents were of analytical purity and were purchased from Sigma-Aldrich Chemical Co. Self-organized TNTs layers were fabricated on a Ti substrate (99.7%, Sigma-Aldrich) by electrochemical anodization in ethylene glycol (anhydrous, 99.8%) electrolyte containing 0.3 M ammonium fluoride (NH<sub>4</sub>F, 98%) and 2 vol % water (H<sub>2</sub>O) using graphite rod as the counter electrode with a potential of 50 V for 3 h. Ti substrates (20 mm × 30 mm × 0.25 mm) were ultrasonically cleaned with acetone and ethanol prior to anodization. The anodized samples were rinsed thoroughly with deionized water and then annealed at 450°C for 1 h. The annealed samples were sonicated in ethanol for 30 min to remove surface debris.

**2.2. Preparation of NiO/TNTs.** An incipient wet impregnation method was adopted for the preparation of NiO/TNTs. The procedure is as follows. TNTs samples were immersed overnight in Ni(NO<sub>3</sub>)<sub>2</sub>·6H<sub>2</sub>O aqueous solution. The molar concentration of Ni(NO<sub>3</sub>)<sub>2</sub>·6H<sub>2</sub>O aqueous solution varied in a range between 0.5 and 2.5 M. This resulted in different concentrations of NiO/TNTs, namely, NiO/TNTs (0.5 M), NiO/TNTs (1.5 M), and NiO/TNTs (2.5 M), respectively. Thus prepared samples were annealed at 450°C for 2 h with a heating rate of 10°C min<sup>-1</sup>. The detailed experiment conditions are shown in Table 1.

**2.3. Characterization of NiO/TNTs.** The morphology and composition of the samples were observed using a field emission scanning electron microscope (FESEM, Auriga, Zeiss) equipped with an energy dispersive X-ray spectroscopy (EDS). The images were obtained at an accelerating voltage of 20 kV. A scanning transmission electron microscope (STEM, SU8000, Hitachi) was carried out at 30 kV to determine

the crystal distribution of NiO/TNTs samples. High resolution transmission electron microscope (HRTEM, Tecnai 20, Philips) images were obtained at 200 kV. The crystalline phase was identified using an X-ray diffractometer (XRD, D8 Advance, Bruker). The target used in the diffractometer is copper (Cu K $\alpha$  radiation,  $\lambda = 1.54 \text{ \AA}$ ). The surface chemical composition of samples was analyzed by X-ray photoelectron spectroscopy (XPS, Axis Ultra DLD, Kratos) with Al K $\alpha$  radiation source. The binding energies were normalized to the signal for adventitious carbon at 284.6 eV. Diffuse reflectance ultraviolet and visible spectra (UV-Vis DRS) were performed using UV-Vis-NIR spectrophotometer (Lambda 750, Perkin Elmer) with a wavelength range of 200–800 nm. Raman shift was recorded with a Raman spectroscopy (RamanMicro 200, Perkin Elmer), ranges in wavelengths from 100 to 700 cm<sup>-1</sup>.

**2.4. Photocatalytic Degradation of Methylene Blue (MB).** The solar-energy-induced photocatalytic activity of NiO/TNTs was evaluated by adopting methylene blue (MB) as a model pollutant under solar light irradiation for 7.5 h. The degradation of MB was carried out in a 1000 mL beaker with the working volume of 200 mL MB solution ( $25 \times 10^{-3} \text{ M}$ ). The prepared samples were loaded in MB solution with only one side faced to solar light irradiation. Prior to the photocatalytic experiment, the dark reaction was carried out for 30 min in order to achieve the adsorption equilibrium. The samples were collected at regular time interval and analyzed for residual MB concentration with visible spectrometer (Spectroquant Pharo 100, Merck) at  $\lambda_{\text{max}} = 664 \text{ nm}$ . The drawn samples were dispensed back into the beaker after the measurement to allow further degradation. The control experiment was performed without a photocatalyst under identical conditions. All experiments were conducted under clear sky conditions at University of Malaya, Kuala Lumpur (latitude 101° 39' E and longitude 3° 7' N), between 11.00 AM and 6.30 PMA in April (2012). Solar light intensity was measured using LT Lutron LX-101 Lux meter of  $1000 \times 100 \text{ lx}$ , and the average light intensity over the duration of clear sky weather condition was found to be 87940 lux (for sunlight AM 1.5,  $100 \text{ mW/cm}^2$  corresponds to 120 000 lux) [35].

## 3. Results and Discussion

**3.1. Structural and Morphological Characterization.** Figures 1(a) and 1(b) show the top and cross-sectional view images of TNTs. The anodized TNTs are covered with surface debris (Figure 1(a)) which can be easily removed by ultrasonication in ethanol for 30 min. TNTs after ultrasonication are shown in Figure 1(b), which reveals that free of surface debris, well-ordered, high-density, and one-dimensional vertically oriented nanotube arrays are formed. The average inner diameter of these nanotubes is 109 nm, nanotube wall thickness is 15 nm and the tube length is in the range of 7–10  $\mu\text{m}$ . The cross-sectional and top view images of the NiO/TNTs are shown in Figures 1(c) and 1(d), respectively. Obviously, the morphological structure of TNTs is not affected by NiO loading. Furthermore, NiO/TNTs samples do

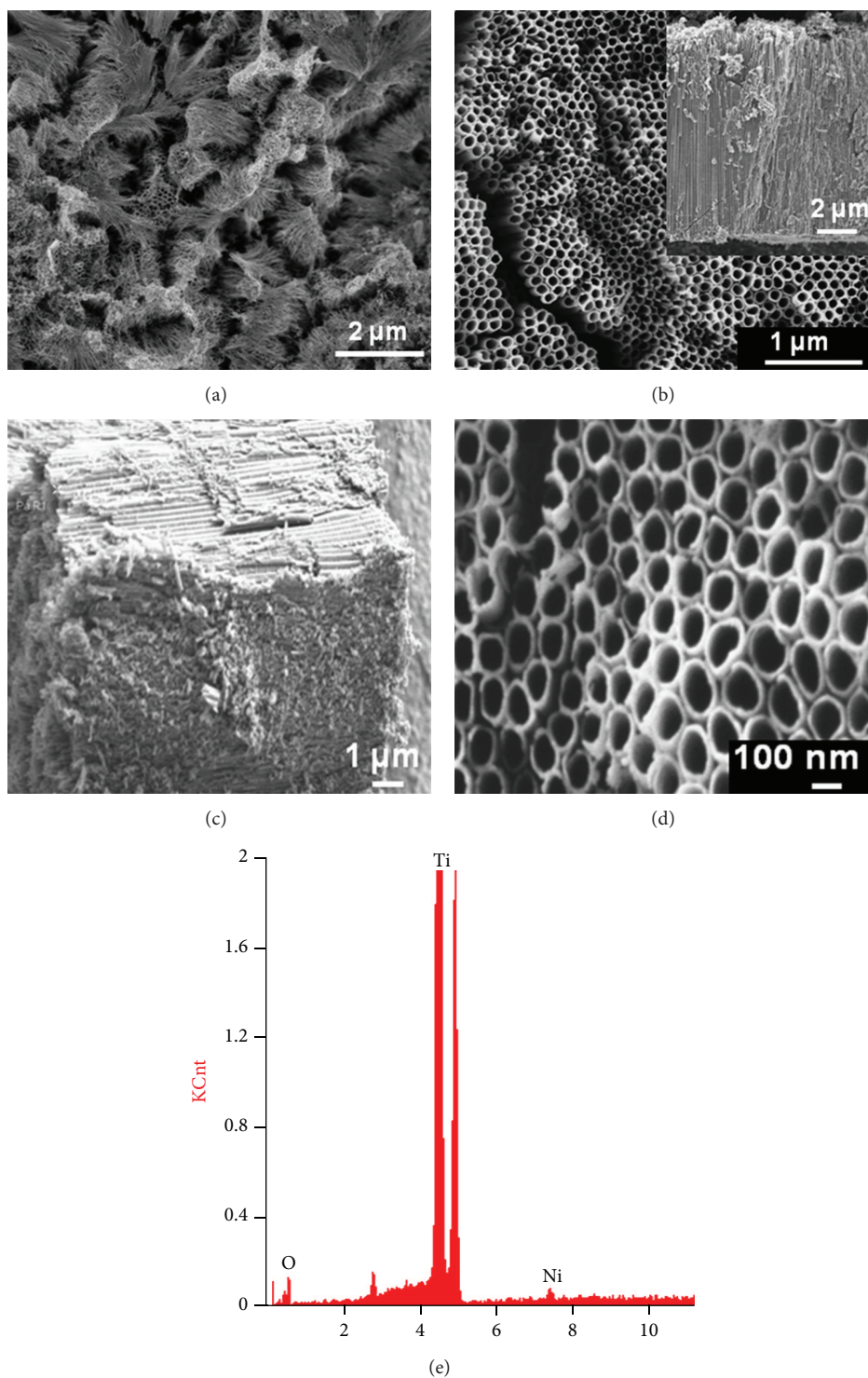


FIGURE 1: (a) FESEM top-view image of TNTs before ultrasonication; (b) top and cross-sectional (inset) images of TNTs after ultrasonication; (c, d) cross-sectional and top-view images of NiO/TNTs (0.5 M); (e) EDX of NiO/TNTs (0.5 M).

not show significant morphological changes with increasing NiO concentration (Figure S1) (see Supplementary Materials available online at <http://dx.doi.org/10.1155/2013/659013>). The EDS analysis in Figure 1(e) depicts the presence of Ni in

TNTs, which is 0.8 wt%, 1 wt%, and 3.4 wt% for 0.5 M, 1.5 M and 2.5 M of NiO/TNTs samples, respectively. The spectrum obtained across the nanotubes over different spots with very reproducible peaks obtained, especially, for Ni ensures

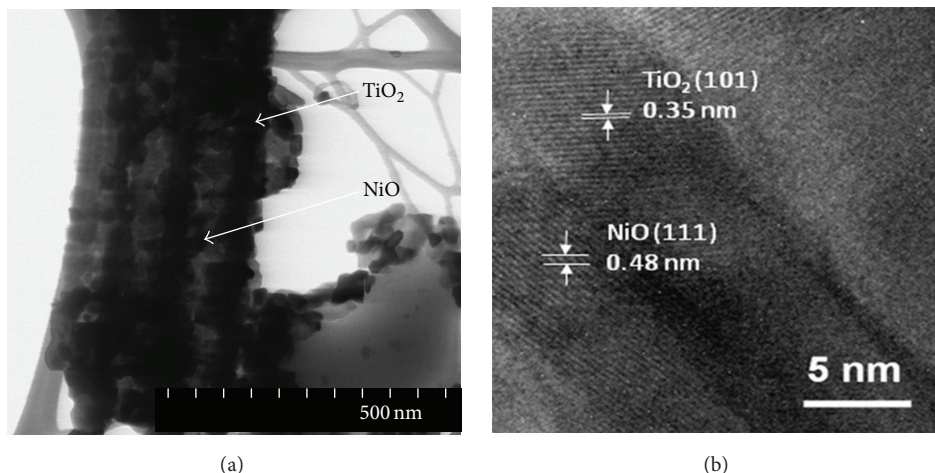


FIGURE 2: (a) STEM image and (b) HRTEM image of NiO/TNTs (0.5 M).

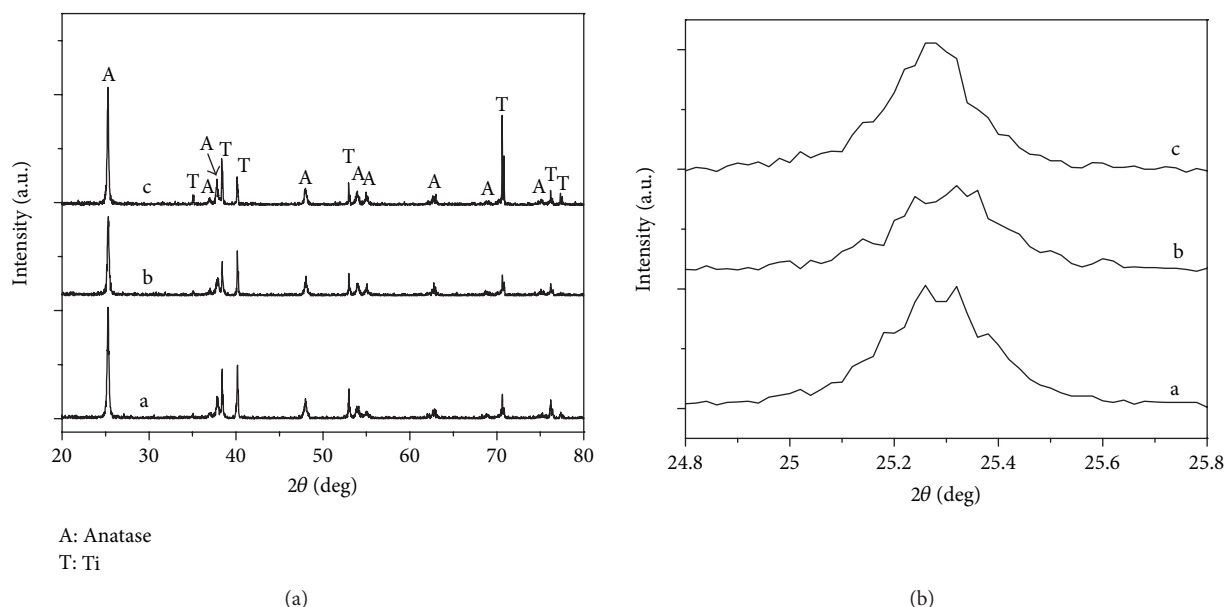


FIGURE 3: (a) X-ray diffraction pattern of photocatalysts (a: TNTs; b: 0.5 M NiO/TNTs; c: 2.5 M NiO/TNTs) and (b) enlarged XRD peaks of crystal plane (1 0 1).

the uniformity of NiO dispersion. Thus, the EDS analysis confirms the presence of Ni in TNTs. The detailed elemental composition is tabulated in Table 1.

STEM measurements are carried out for distribution analysis of NiO nanoparticles throughout the TNTs surface. Figure 2(a) shows the STEM image of NiO nanoparticles along with size distribution ( $\sim 29.8$ – $40.6$  nm) inside the walls of TNTs. Bright-field and dark-field images (Figure S2) indicate the presence of nanosized NiO particles inside the hollow structure of nanotubes. No nanoparticles were detected on the top openings of nanotubes (Figure S3), instead they were located along the walls of the TNTs. HRTEM pattern of NiO/TNTs is obtained to verify the crystallization of nanotubes. Direct evidence of crystalline nature of NiO

and TiO<sub>2</sub> is observed in Figure 2(b). The lattice spacing of two lattice planes with spacing of 0.35 nm and 0.48 nm, corresponding to the (1 0 1) plane of anatase TiO<sub>2</sub> (JCPDS no. 21-1272) and (1 1 1) plane of NiO (JCPDS no. 89-5881) is observed clearly.

Figure 3(a) shows the XRD patterns of NiO/TNTs compared to that of TNTs. All diffraction peaks can be assigned as 100% anatase TiO<sub>2</sub> and Ti substrate, which reveals that there has been virtually no phase change in TiO<sub>2</sub> after the loading of NiO, irrespective of the concentration of NiO. The peaks of tetragonal TiO<sub>2</sub> anatase phase (JCPDS no. 21-1272) appeared at 25.3°, 36.9°, 37.8°, 48.0°, 53.9°, 55.1°, 62.7°, 68.8°, and 75.0°, corresponding to (1 0 1), (1 0 3), (0 0 4), (2 0 0), (1 0 5), (2 1 1), (2 0 4), (1 1 6), and (2 1 5) crystal planes,

TABLE 2: Lattice parameters for TNTs and NiO/TNTs samples with different concentrations.

| Sample           | Crystallite size (nm) <sup>a</sup> | Cell parameters<br>$a = b, c$ (Å) <sup>b</sup> |
|------------------|------------------------------------|--|
| TNTs             | 33.81                              | 3.7868, 9.5102                                 |
| NiO/TNTs (0.5 M) | 34.54                              | 3.7828, 9.5184                                 |
| NiO/TNTs (2.5 M) | 34.10                              | 3.7872, 9.5438                                 |

<sup>a</sup> Measured by Scherrer's equation.

<sup>b</sup> Estimated according to (2) and (3).

respectively. The Ti peaks are also observed which belong to Ti substrate underneath the oxide nanostructure layer. No new peaks associated with crystalline phases of NiO were detected. This could be explained by the following reasons: (i) Ni cations (0.72 Å) are well substituted into the Ti cations (0.68 Å) in anatase TiO<sub>2</sub> lattice due to their similar ionic radii; (ii) the formation of NiO is below the XRD detection limit due to the presence of NiO in low concentration; (iii) well and uniform dispersion of NiO particles on TiO<sub>2</sub> surface [36, 37]. The lattice parameters and crystallite size of all samples are calculated using the formula stated below and are summarized in Table 2. The average crystallite sizes of TiO<sub>2</sub> anatase were calculated using Scherrer's equation:

$$D = \frac{K\lambda}{\beta \cos \theta}, \quad (1)$$

where  $\beta$  is the full width half maximum (FWHM) for the  $2\theta$  peak,  $K$  is the shape factor taken as 0.89 for calculations,  $\lambda$  is the wavelength of X-ray (0.154 nm), and  $\theta$  is the diffraction angle. The lattice parameters were measured using (1 0 1) and (2 0 0) in anatase crystal planes by using Bragg's equations:

$$d_{(hkl)} = \frac{\lambda}{2 \sin \theta}. \quad (2)$$

Formula for tetragonal system is as follows:

$$\left(d_{hkl}^{-2}\right) = h^2 a^{-2} + k^2 b^{-2} + l^2 c^{-2}, \quad (3)$$

where  $d_{(hkl)}$  is the distance between crystal planes of  $(hkl)$ ,  $\lambda$  is the X-ray wavelength,  $\theta$  is the diffraction angle of crystal plane  $(hkl)$ ,  $(hkl)$  is the crystal index, and  $a$ ,  $b$ , and  $c$  are lattice parameters (in anatase form,  $a = b \neq c$ ).

The lattice parameters of all samples remain almost unchanged along  $a$ - and  $b$ -axis, whereas the  $c$ -axis parameter undergoes a minor increase with increasing NiO concentrations. The XRD results are correlated to XPS analysis in Figure 6(b). It reveals that a large fraction of Ni<sup>2+</sup> ions segregates as a separate NiO and as a major phase, while the remainder fraction is incorporated substitutionally in TiO<sub>2</sub> lattice. As evidence, the Ti 2p XPS spectra in Figure 6(b) could only detect the presence of Ti<sup>4+</sup> in TiO<sub>2</sub>, and there is no apparent peak broadening in the XRD patterns of NiO/TNTs (Figure 3(b)). The slight increase of  $c$ -axis parameter with increasing NiO concentrations (Table 2) suggested that minor fraction of Ni<sup>2+</sup> replaces Ti<sup>4+</sup>. This was achieved

due to similar ionic radius of both Ni<sup>2+</sup> (0.72 Å) and Ti<sup>4+</sup> (0.68 Å) [38]. It is also speculated that Ni<sup>2+</sup> was not incorporated interstitially because the lattice constants did not remain constant for higher NiO concentrations. Upon the NiO loading to 2.5 M (Table 2), the crystallite size of NiO/TNTs (34.54 nm) is larger than that of TNTs (33.81 nm). The increase in crystallite size suggests that NiO loading does not lead to the suppression of TiO<sub>2</sub> crystal growth.

**3.2. Raman Spectra.** Raman spectra of TNTs and NiO/TNTs are depicted in Figure 4(a). 2.5 M NiO/TNTs sample yields four distinct Raman peaks at 145 ( $E_g$ ), 399 ( $B_{1g}$ ), 519 ( $A_{1g} + B_{1g}$ ), and 639 cm<sup>-1</sup> ( $E_g$ ) with slight broadening, as compared with the other two samples. These are directly attributable to the anatase phase. The broadening of Raman spectra at 145 cm<sup>-1</sup> (Figure 4(b)) implies the breakdown of long-range translational crystal symmetry, owing to the substitution of Ni ions into the TiO<sub>2</sub> lattice [39]. The absence of NiO or other oxidation state of Ni related modes in the Raman spectra is in good agreement with XRD results.

**3.3. UV-Vis Diffuse Reflectance Spectra.** The prior challenge in improving the properties of titania is to shift the absorption spectrum of TiO<sub>2</sub> towards the visible region for efficient solar light photons harvesting. The diffuse reflectance spectra (DRS) of different concentrations of NiO/TNTs and TNTs samples are shown in Figure 5. All samples exhibit an absorption band lower than 380 nm (UV region) due to the charge transfer from O 2p valence band to Ti 3d conduction band [40].

It can be seen that NiO/TNTs (0.5 M) did not show a significant red-shifted absorption edge towards visible region due to its marginal increase of NiO concentrations compared to that of TNTs. Meanwhile, the further increasing of NiO concentrations up to 1.5 M and 2.5 M results in a drastic shift towards the visible region. Sample NiO/TNTs (2.5 M) shows a distinct hump between 450 and 515 nm which is due to the crystal field splitting of 3d<sup>8</sup> orbital and charge transfer from Ni<sup>2+</sup> to Ti<sup>4+</sup>, respectively [41]. In the junction region of NiO/TNTs, the overlap of conduction band of 3d level in Ti<sup>4+</sup> with d-level of Ni<sup>2+</sup> enables charge transfer transitions between electrons in d-level of Ni<sup>2+</sup> and the conduction band of TiO<sub>2</sub>. It also decreases the energy gap between Ti 3d and O 2p states of TiO<sub>2</sub> [41, 42] and facilitates absorption in visible spectrum. This reveals the good contact in between NiO and TiO<sub>2</sub> in consequence of the interdispersion of the two oxides [32].

**3.4. XPS Analysis.** High-resolution XPS was performed to determine the chemical composition and the oxidation state for NiO/TNTs samples. The fully scanned XPS spectra (Figure 6(a)) indicate that Ti, O, and Ni elements exist in NiO/TNTs heterostructures. XPS of Ni 2p, O 1s and Ti 2p core levels of the NiO/TNTs exist as (1) Ti 2p region (450–470 eV); (2) Ni 2p region (850–890 eV); and (3) O 1s region (520–540 eV). Peak fitting to the spectra was applied using Gaussian-Lorentzian peak shape after subtraction of Shirley background. As shown in Figure 6(b), there are two peaks

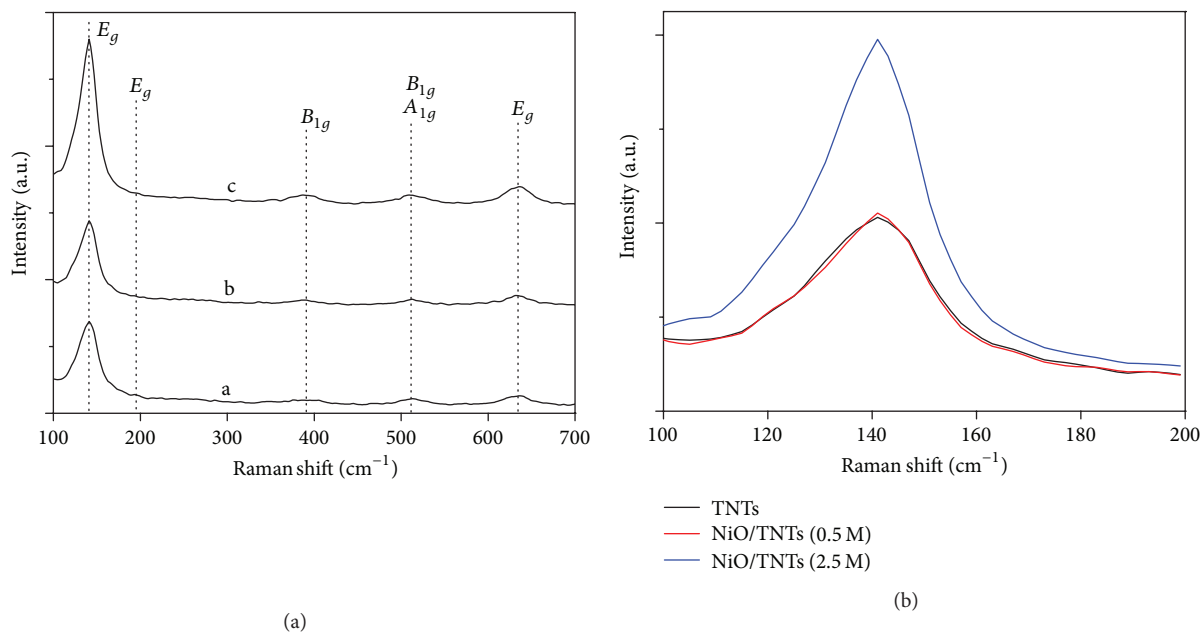


FIGURE 4: (a) Raman spectra of photocatalysts (a: TNTs; b: 0.5 M NiO/TNTs; c: 2.5 M NiO/TNTs) and (b) enlarged region of Raman shift range 100–200 cm<sup>-1</sup>.

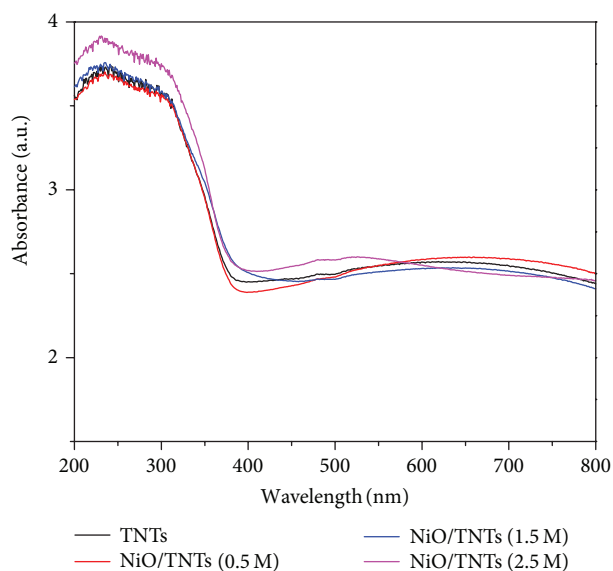


FIGURE 5: UV-Visible absorption spectra of pure TNTs and different concentrations of NiO/TNTs (concentrations in molarity).

observed at 458.4 eV (Ti 2p<sub>3/2</sub>) and 464.1 eV (Ti 2p<sub>1/2</sub>), and both correspond to Ti<sup>4+</sup> in TiO<sub>2</sub> [43].

The high-resolution XPS of O 1s core level can be fitted to four kinds of chemical states (Figure 6(c)). The peaks at 529.7, 530.8, 531.9, and 533.2 eV can be associated with oxygen in TiO<sub>2</sub>, NiO, Ni<sub>2</sub>O<sub>3</sub>, and adsorbed water, respectively. The Ni 2p XPS spectra in Figure 6(d) were fitted into four peaks including NiO (2p<sub>3/2</sub>), NiO (2p<sub>1/2</sub>), Ni<sub>2</sub>O<sub>3</sub> (2p<sub>3/2</sub>), and Ni<sub>2</sub>O<sub>3</sub> (2p<sub>1/2</sub>). The binding energy of 855.6 eV and 873.1 eV

corresponds to Ni<sup>2+</sup> in NiO [44], and the binding energies of 856.3 eV and 874.1 eV indicate the presence of Ni<sup>3+</sup> in Ni<sub>2</sub>O<sub>3</sub> [17]. A detailed surface elemental compositions of NiO/TNTs (0.5 M) detected by XPS is summarized in Table S1.

**3.5. Photocatalytic Activity NiO/TNTs.** Figure 7(a) shows the solar-light-induced photocatalytic activity of the NiO/TNTs. The initial concentration ( $C_0$ ) is the MB concentration after adsorption-desorption equilibrium. Irrespective of NiO concentrations from 50.8 to 51.7% of dye is removed under dark conditions (30 min). The good adsorption capability of NiO/TNTs is attributed to the large surface area, which enables the MB molecules to diffuse freely inside NiO/TNTs [45]. 43.25% of the MB was removed in the control experiment. The photocatalytic reactions for all samples followed pseudo-first-order reaction kinetics, which is expressed by

$$\ln\left(\frac{C_0}{C}\right) = kt, \quad (4)$$

where  $k$  is the first-order reaction constant,  $C_0$  and  $C$  are the initial and the final concentrations of MB dye, respectively. The kinetic plot and photocatalytic results are shown in Figure 7(b) and Table 3, respectively.

All NiO/TNTs samples show higher degradation efficiency than TNTs. The loading of NiO in TNTs resulted in a doubled reaction rate (0.004 min<sup>-1</sup>) with 86% of MB removal than that of pure TNTs ( $k = 0.002$  min<sup>-1</sup>) with 68% MB removal. In the initial, NiO/TNTs (2.5 M) shows higher reaction rate than NiO/TNTs samples with lower concentrations (0.5 M and 1.5 M). This could be contributed to the distinct hump observed in the diffuse reflectance spectra (Figure 5) of NiO/TNTs (2.5 M). However, the solar-light-induced activities of all NiO/TNTs samples start to slow

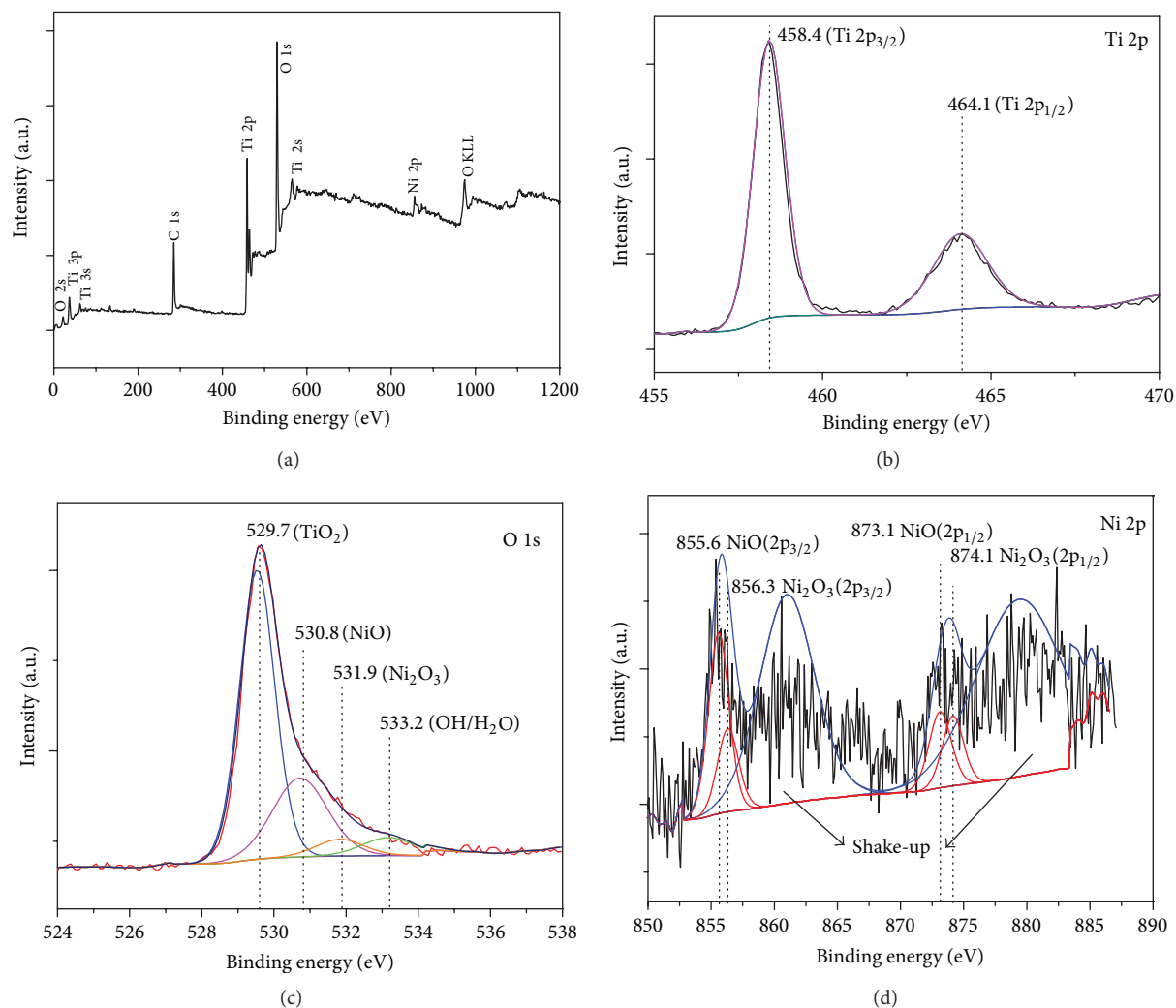


FIGURE 6: XPS spectra of NiO/TNTs (0.5 M) (a) fully scanned spectra, (b) Ti 2p peak, (c) O 1s peak, and (d) Ni 2p peak.

down and reach an identical MB degradation (86%) towards the end of reaction. The increase in degradation efficiency of NiO/TNTs is mainly due to the efficient electron-hole pairs separation and visible light absorption. The presence of NiO develops a p-n junction to separate electron-hole pairs effectively, while the visible-light property is due to charge transfer transition from the electron donor levels formed by the 3d orbitals of substituted  $\text{Ni}^{2+}$  to the conduction bands of  $\text{TiO}_2$  [46]. Further,  $\text{Ni}_2\text{O}_3$  has a dark colour, and it facilitates the absorption of visible light [17]. The other contributing factor is the presence of  $\text{Ni}_2\text{O}_3$  which creates  $\text{Ni}^{2+}$  vacancies in NiO which can lower the electrical resistance of NiO [44].

A competitive adsorption on the active sites between the reactant and the intermediate products reduces the degradation rate towards the end of reaction [47]. Hence, the accessibility of reactant to the active sites is affected resulting in a nonsignificant difference of degradation efficiency for all NiO/TNTs samples when reactions end. In addition, the similar Ni content in 0.5 M NiO/TNTs (0.8 wt%) and 1.5 M

NiO/TNTs (1 wt%) could also result in a nonsignificant difference of degradation rate for both samples. Overall, it can be concluded that the loading of NiO effectively improve solar-light-induced photoactivity. Though NiO/TNTs with higher NiO concentration possess better visible-light absorption properties, it has no direct effect on the enhancement of photocatalytic activity (Figure 5).

**3.6. Degradation Mechanism.** The degradation mechanism of MB over NiO/TNTs and the effect of p-n-junction are illustrated in Figure 8. In presence of solar irradiation, the electrons are excited from valence band of  $\text{TiO}_2$  to the conduction band. As indicated in XRD and XPS results, a major part of  $\text{Ni}^{2+}$  ions segregates as separate NiO nanoparticles on the surface of TNTs, whereas the remainder portion is incorporated substitutionally in  $\text{TiO}_2$  lattice. When segregated NiO nanoparticles and  $\text{TiO}_2$  integrate, a p-n-junction will be formed between p-type NiO (p-NiO) and n-type  $\text{TiO}_2$  (n- $\text{TiO}_2$ ). At the equilibrium, the negative charge and

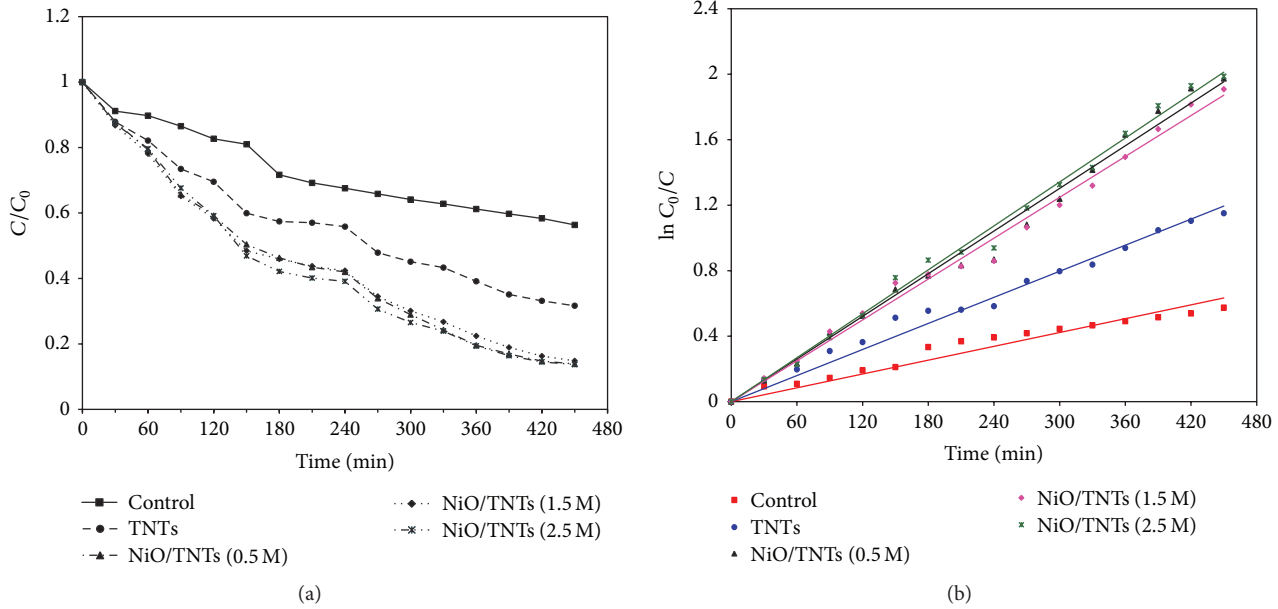


FIGURE 7: (a) Photocatalytic degradation of MB over TNTs samples with varying NiO concentrations under solar light irradiation and (b) kinetic plot of TNTs samples with varying NiO concentrations.

TABLE 3: Photodegradation of MB dye for TNTs and NiO/TNTs samples under solar light irradiation.

| Sample               | MB degraded <sup>a</sup><br>( $C_0 - C$ )/ $C_0$ (%) | $k^b$ ( $\text{min}^{-1}$ ) |
|----------------------|--|-----------------------------|
| Control <sup>c</sup> | 43.65  | 0.001                       |
| TNTs                 | 68.35  | 0.002                       |
| NiO/TNTs (0.5 M)     | 86.11  | 0.004                       |
| NiO/TNTs (1.5 M)     | 86.18  | 0.004                       |
| NiO/TNTs (2.5 M)     | 86.29  | 0.004                       |

<sup>a</sup> After reaction for 7.5 h.

<sup>b</sup> Apparent rate constant deduced from linear fitting of  $\ln(C_0/C)$  versus reaction time.

<sup>c</sup> The control was the photolysis of MB dye.

positive charge will be formed in p-NiO region and n-TiO<sub>2</sub> region, respectively. When the p-n junction is irradiated by photons, the photogenerated holes flow to valence band of NiO nanoparticles (negative field), while the electrons flow to conduction band of TiO<sub>2</sub> (positive field) [31, 33]. Therefore, the electrons on the TiO<sub>2</sub> surface are scavenged by the oxygen (O<sub>2</sub>) adsorbed on TiO<sub>2</sub> surface or dissolved oxygen in MB solution to produce superoxide radical anion O<sub>2</sub><sup>•-</sup> [47]. Meanwhile, the photogenerated holes in valence band of NiO nanoparticles oxidize the organic molecule in MB solution to form R<sup>+</sup> or react with OH<sup>-</sup> or H<sub>2</sub>O then oxidizing them into •OH radicals. When Ti<sup>4+</sup> in TiO<sub>2</sub> lattice is replaced with Ni<sup>2+</sup>, the overlap of the conduction band of 3d level in Ti<sup>4+</sup> with d-level of Ni ions [42] can induce the charge transfer transitions between Ni<sup>2+</sup> d electrons and the conduction band of TiO<sub>2</sub> at lower bandgap energy. An electron is excited at this lower energy level into TiO<sub>2</sub> conduction band and further react

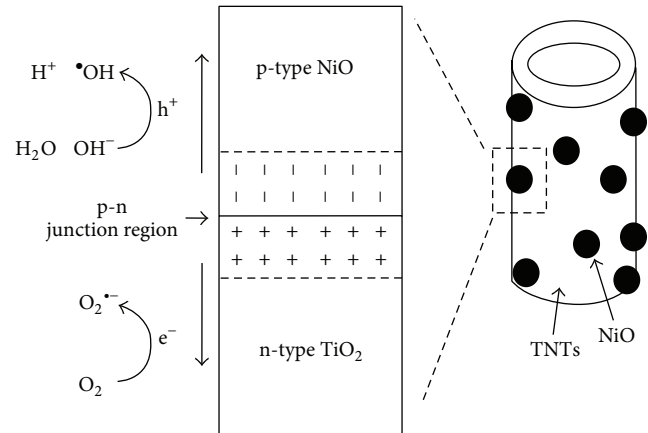


FIGURE 8: Schematic diagram of electron transport in NiO/TNTs photocatalyst under solar light irradiation.

with O<sub>2</sub> adsorbed on TiO<sub>2</sub> surface, leading to the formation of •OH radicals. The resulting •OH radicals are strong oxidizing agent (standard redox potential +2.8 V) which can actively oxidize MB dye.

#### 4. Conclusions

Self-organized and vertically oriented TNTs were successfully loaded with NiO nanoparticles. XRD and XPS results reveal that a large part of Ni<sup>2+</sup> ions segregate as a separate NiO and as a major phase, and the remaining part is incorporated substitutionally in TiO<sub>2</sub> lattice. Both the TNTs and NiO/TNTs photocatalysts possess large surface area which facilitates diffusion of MB molecules inside channel of

samples and hence enhances its adsorption capability. Solar-energy-induced photocatalytic activity showed the degradation rate of MB is independent of NiO concentration. Overall, the NiO/TNTs samples exhibited higher degradation efficiency compared to that of TNTs.

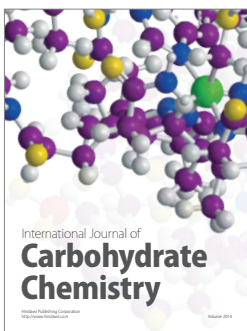
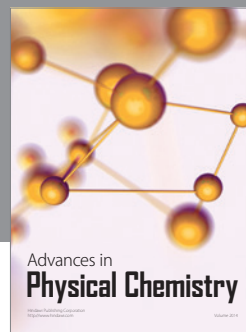
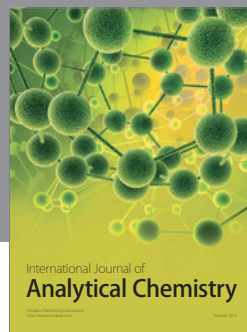
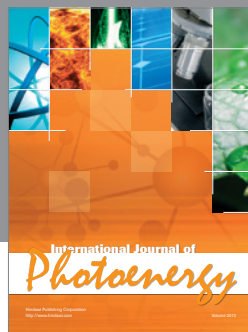
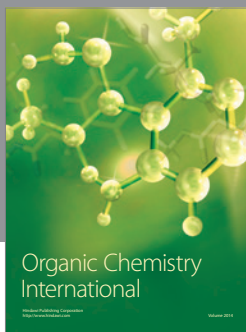
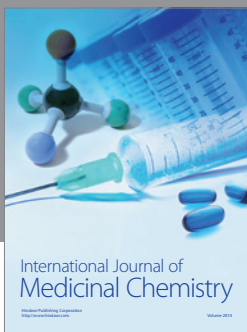
## Acknowledgments

This work was supported by University of Malaya Research Grant (RG167/12SUS) and Postgraduate Research Grant (PVI06/2012A), respectively. The authors are grateful to Advance Materials Research Centre (AMREC) and Low Dimensional Materials Research Centre (LDMRC), University of Malaya, in assisting in characterization works.

## References

- [1] K. Xie, L. Sun, C. Wang et al., "Photoelectrocatalytic properties of Ag nanoparticles loaded TiO<sub>2</sub> nanotube arrays prepared by pulse current deposition," *Electrochimica Acta*, vol. 55, no. 24, pp. 7211–7218, 2010.
- [2] H. An, J. Zhou, J. Li et al., "Deposition of Pt on the stable nanotubular TiO<sub>2</sub> and its photocatalytic performance," *Catalysis Communications*, vol. 11, no. 3, pp. 175–179, 2009.
- [3] S. K. Mohapatra, N. Kondamudi, S. Banerjee, and M. Misra, "Functionalization of self-organized TiO<sub>2</sub> nanotubes with Pd nanoparticles for photocatalytic decomposition of dyes under solar light illumination," *Langmuir*, vol. 24, no. 19, pp. 11276–11281, 2008.
- [4] O. K. Varghese, M. Paulose, T. J. LaTempa, and C. A. Grimes, "High-rate solar photocatalytic conversion of CO<sub>2</sub> and water vapor to hydrocarbon fuels," *Nano Letters*, vol. 9, no. 2, pp. 731–737, 2009.
- [5] J. Wang and Z. Lin, "Dye-sensitized TiO<sub>2</sub> nanotube solar cells with markedly enhanced performance via rational surface engineering," *Chemistry of Materials*, vol. 22, no. 2, pp. 579–584, 2010.
- [6] Y. Sun, G. X. Wang, and K. P. Yan, "TiO<sub>2</sub> nanotubes for hydrogen generation by photocatalytic water splitting in a two compartment photoelectrochemical cell," *International Journal of Hydrogen Energy*, vol. 36, no. 24, pp. 15502–15508, 2011.
- [7] Y. Liu, C. S. Xie, H. Y. Li, H. Chen, T. Zou, and D. W. Zeng, "Improvement of gaseous pollutant photocatalysis with WO<sub>3</sub>/TiO<sub>2</sub> heterojunctional-electrical layered system," *Journal of Hazardous Materials*, vol. 196, pp. 52–58, 2011.
- [8] S. Malato, P. Fernández-Ibáñez, M. I. Maldonado, J. Blanco, and W. Gernjak, "Decontamination and disinfection of water by solar photocatalysis: recent overview and trends," *Catalysis Today*, vol. 147, no. 1, pp. 1–59, 2009.
- [9] B. Wawrzyniak, A. W. Morawski, and B. Tryba, "Preparation of TiO<sub>2</sub>-nitrogen-doped photocatalyst active under visible light," *International Journal of Photoenergy*, vol. 2006, Article ID 68248, 8 pages, 2006.
- [10] L. P. Wen, B. S. Liu, X. J. Zhao, K. Nakata, T. Murakami, and A. Fujishima, "Synthesis, characterization, and photocatalysis of Fe-Doped TiO<sub>2</sub>: a combined experimental and theoretical study," *International Journal of Photoenergy*, vol. 2012, Article ID 368750, 10 pages, 2012.
- [11] X. J. Feng, J. D. Sloppy, T. J. LaTempa et al., "Synthesis and deposition of ultrafine Pt nanoparticles within high aspect ratio TiO<sub>2</sub> nanotube arrays: application to the photocatalytic reduction of carbon dioxide," *Journal of Materials Chemistry*, vol. 21, pp. 13429–13433, 2011.
- [12] N. Sasirekha, S. J. S. Basha, and K. Shanthi, "Photocatalytic performance of Ru doped anatase mounted on silica for reduction of carbon dioxide," *Applied Catalysis B*, vol. 62, no. 1-2, pp. 169–180, 2006.
- [13] G. Yang, Z. Jiang, H. Shi, T. Xiao, and Z. Yan, "Preparation of highly visible-light active N-doped TiO<sub>2</sub> photocatalyst," *Journal of Materials Chemistry*, vol. 20, no. 25, pp. 5301–5309, 2010.
- [14] W. J. Zhang, B. Yang, and J. L. Chen, "Effects of calcination temperature on preparation of boron-doped TiO<sub>2</sub> by sol-gel method," *International Journal of Photoenergy*, vol. 2012, Article ID 528637, 8 pages, 2012.
- [15] G. Yan, M. Zhang, J. Hou, and J. Yang, "Photoelectrochemical and photocatalytic properties of N + S co-doped TiO<sub>2</sub> nanotube array films under visible light irradiation," *Materials Chemistry and Physics*, vol. 129, no. 1-2, pp. 553–557, 2011.
- [16] Y. F. Lee, K. H. Chang, C. C. Hu, and K. M. Lin, "Synthesis of activated carbon-surrounded and carbon-doped anatase TiO<sub>2</sub> nanocomposites," *Journal of Materials Chemistry*, vol. 20, no. 27, pp. 5682–5688, 2010.
- [17] N. K. Shrestha, M. Yang, Y. C. Nah, I. Paramasivam, and P. Schmuki, "Self-organized TiO<sub>2</sub> nanotubes: visible light activation by Ni oxide nanoparticle decoration," *Electrochemistry Communications*, vol. 12, no. 2, pp. 254–257, 2010.
- [18] J. Wang, Z. Jiang, L. Zhang et al., "Sonocatalytic degradation of some dyestuffs and comparison of catalytic activities of nano-sized TiO<sub>2</sub>, nano-sized ZnO and composite TiO<sub>2</sub>/ZnO powders under ultrasonic irradiation," *Ultrasonics Sonochemistry*, vol. 16, no. 2, pp. 225–231, 2009.
- [19] D. L. He, M. D. Chen, F. Teng et al., "Enhanced cyclability of CdS/TiO<sub>2</sub> photocatalyst by stable interface structure," *Superlattices and Microstructures*, vol. 51, no. 6, pp. 799–808, 2012.
- [20] Q. Kang, S. Liu, L. Yang, Q. Cai, and C. A. Grimes, "Fabrication of PbS nanoparticle-sensitized TiO<sub>2</sub> nanotube arrays and their photoelectrochemical properties," *ACS Applied Materials & Interfaces*, vol. 3, no. 3, pp. 746–749, 2011.
- [21] H. A. Hamedani, N. K. Allam, H. Garmestani, and M. A. El-Sayed, "Electrochemical fabrication of strontium-doped TiO<sub>2</sub> nanotube array electrodes and investigation of their photoelectrochemical properties," *The Journal of Physical Chemistry C*, vol. 115, no. 27, pp. 13480–13486, 2011.
- [22] H. A. J. L. Mourão, W. A. Junior, and C. Ribeiro, "Hydrothermal synthesis of Ti oxide nanostructures and TiO<sub>2</sub>:SnO<sub>2</sub> heterostructures applied to the photodegradation of rhodamine B," *Materials Chemistry and Physics*, vol. 135, no. 2-3, pp. 524–532, 2012.
- [23] T. Sreethawong, Y. Suzuki, and S. Yoshikawa, "Photocatalytic evolution of hydrogen over mesoporous TiO<sub>2</sub> supported NiO photocatalyst prepared by single-step sol-gel process with surfactant template," *International Journal of Hydrogen Energy*, vol. 30, no. 10, pp. 1053–1062, 2005.
- [24] J. Guo, W. Fu, H. Yang et al., "A NiO/TiO<sub>2</sub> junction electrode constructed using self-organized TiO<sub>2</sub> nanotube arrays for highly efficient photoelectrocatalytic visible light activations," *Journal of Physics D*, vol. 43, no. 24, Article ID 245202, 2010.
- [25] H. Y. Lin, Y. F. Chen, and Y. W. Chen, "Water splitting reaction on NiO/InVO<sub>4</sub> under visible light irradiation," *International Journal of Hydrogen Energy*, vol. 32, no. 1, pp. 86–92, 2007.

- [26] A. Hameed, T. Montini, V. Gombaca, and P. Fornasiero, "Photocatalytic decolourization of dyes on NiO–ZnO nanocomposites," *Photochemical and Photobiological Sciences*, vol. 8, pp. 677–682, 2009.
- [27] S. M. Chang and W. S. Liu, "Surface doping is more beneficial than bulk doping to the photocatalytic activity of vanadium-doped TiO<sub>2</sub>," *Applied Catalysis B*, vol. 101, no. 3–4, pp. 333–342, 2011.
- [28] H. Sato, T. Minami, S. Takata, and T. Yamada, "Transparent conducting p-type NiO thin films prepared by magnetron sputtering," *Thin Solid Films*, vol. 236, no. 1–2, pp. 27–31, 1993.
- [29] A. Hameed and M. A. Gondal, "Production of hydrogen-rich syngas using p-type NiO catalyst: a laser-based photocatalytic approach," *Journal of Molecular Catalysis A*, vol. 233, no. 1–2, pp. 35–41, 2005.
- [30] Z. Zhang, C. Shao, X. Li, C. Wang, M. Zhang, and Y. Liu, "Electrospun nanofibers of p-type NiO/n-type ZnO heterojunctions with enhanced photocatalytic activity," *ACS Applied Materials and Interfaces*, vol. 2, no. 10, pp. 2915–2923, 2010.
- [31] S. F. Chan, S. J. Zhang, W. Liu, and W. Zhao, "Preparation and activity evaluation of p-n junction photocatalyst NiO/TiO<sub>2</sub>," *Journal of Hazardous Materials*, vol. 155, no. 1–2, pp. 320–326, 2008.
- [32] Y. Ku, C. N. Lin, and W. M. Hou, "Characterization of coupled NiO/TiO<sub>2</sub> photocatalyst for the photocatalytic reduction of Cr(VI) in aqueous solution," *Journal of Molecular Catalysis A*, vol. 349, no. 1–2, pp. 20–27, 2011.
- [33] Y. Chen, J. C. Crittenden, S. Hackney, L. Sutter, and D. W. Hand, "Preparation of a novel TiO<sub>2</sub>-based p-n junction nanotube photocatalyst," *Environmental Science and Technology*, vol. 39, no. 5, pp. 1201–1208, 2005.
- [34] D. W. Hwang, H. G. Kim, J. Kim, K. Y. Cha, Y. G. Kim, and J. S. Lee, "Photocatalytic water splitting over highly donor-doped (110) layered perovskites," *Journal of Catalysis*, vol. 193, no. 1, pp. 40–48, 2000.
- [35] H. Pettersson and T. Gruszecki, "Long-term stability of low-power dye-sensitised solar cells prepared by industrial methods," *Solar Energy Materials and Solar Cells*, vol. 70, no. 2, pp. 203–212, 2001.
- [36] B. K. Vijayan, N. M. Dimitrijevic, J. Wu, and K. A. Gray, "The effects of Pt doping on the structure and visible light photoactivity of titania nanotubes," *Journal of Physical Chemistry C*, vol. 114, no. 49, pp. 21262–21269, 2010.
- [37] Q. Li and J. K. Shang, "Composite photocatalyst of nitrogen and fluorine codoped titanium oxide nanotube arrays with dispersed palladium oxide nanoparticles for enhanced visible light photocatalytic performance," *Environmental Science and Technology*, vol. 44, no. 9, pp. 3493–3499, 2010.
- [38] D. H. Kim, H. S. Park, S. J. Kim, and K. S. Lee, "Synthesis of novel TiO<sub>2</sub> by mechanical alloying and heat treatment-derived nanocomposite of TiO<sub>2</sub> and NiTiO<sub>3</sub>," *Catalysis Letters*, vol. 106, no. 1–2, pp. 29–33, 2006.
- [39] M. Pal, U. Pal, J. M. G. Y. Jiménez, and F. Pérez-Rodríguez, "Effects of crystallization and dopant concentration on the emission behavior of TiO<sub>2</sub>:Eu nanophosphors," *Nanoscale Research Letters*, vol. 7, pp. 1–12, 2012.
- [40] A. Fuerte, M. D. Hernández-Alonso, A. J. Maira et al., "Nanosize Ti–W mixed oxides: effect of doping level in the photocatalytic degradation of toluene using sunlight-type excitation," *Journal of Catalysis*, vol. 212, no. 1, pp. 1–9, 2002.
- [41] Y. J. Lin, Y. H. Chang, W. D. Yang, and B. S. Tsai, "Synthesis and characterization of ilmenite NiTiO<sub>3</sub> and CoTiO<sub>3</sub> prepared by a modified Pechini method," *Journal of Non-Crystalline Solids*, vol. 352, no. 8, pp. 789–794, 2006.
- [42] G. K. Mor, H. E. Prakasam, O. K. Varghese, K. Shankar, and C. A. Grimes, "Vertically oriented Ti–Fe–O nanotube array films: toward a useful material architecture for solar spectrum water photoelectrolysis," *Nano Letters*, vol. 7, no. 8, pp. 2356–2364, 2007.
- [43] H. J. Choi and M. Kang, "Hydrogen production from methanol/water decomposition in a liquid photosystem using the anatase structure of Cu loaded TiO<sub>2</sub>," *International Journal of Hydrogen Energy*, vol. 32, no. 16, pp. 3841–3848, 2007.
- [44] B. Sasi and K. G. Gopchandran, "Nanostructured mesoporous nickel oxide thin films," *Nanotechnology*, vol. 18, no. 11, Article ID 115613, 2007.
- [45] M. A. Ahmed, "Synthesis and structural features of mesoporous NiO/TiO<sub>2</sub> nanocomposites prepared by sol-gel method for photodegradation of methylene blue dye," *Journal of Photochemistry and Photobiology A*, vol. 238, pp. 63–70, 2012.
- [46] R. Niishiro, H. Kato, and A. Kudo, "Nickel and either tantalum or niobium-codoped TiO<sub>2</sub> and SrTiO<sub>3</sub> photocatalysts with visible-light response for H<sub>2</sub> or O<sub>2</sub> evolution from aqueous solutions," *Physical Chemistry Chemical Physics*, vol. 7, no. 10, pp. 2241–2245, 2005.
- [47] I. K. Konstantinou and T. A. Albanis, "TiO<sub>2</sub>-assisted photocatalytic degradation of azo dyes in aqueous solution: kinetic and mechanistic investigations: a review," *Applied Catalysis B*, vol. 49, no. 1, pp. 1–14, 2004.



**Hindawi**

Submit your manuscripts at  
<http://www.hindawi.com>

